International Journal of Mass Spectrometry 414 (2017) 13–22

Contents lists available at ScienceDirect

International Journal of Mass Spectrometry

journal homepage: www.elsevier.com/locate/ijms

Computation of Mathieu stability plot for an arbitrary toroidal ion trap mass analyser

Appala Naidu Kotana [a], Atanu K. Mohanty [a,b,*]

[a] Department of Computational and Data Sciences, Indian Institute of Science, Bangalore 560012, India
[b] Department of Instrumentation and Applied Physics, Indian Institute of Science, Bangalore 560012, India

ARTICLE INFO

Article history:
Received 13 October 2016
Received in revised form
22 November 2016
Accepted 23 November 2016
Available online 5 December 2016

Keywords:
Toroidal ion trap
Toroidal multipole coefficients
Mathieu parameters
Mathieu stability plot
Secular frequency
Nonlinear resonances

ABSTRACT

This paper presents a method to construct Mathieu stability plot for any arbitrary toroidal ion trap mass analyser. The proposed method is demonstrated on two toroidal ion trap mass analyser geometries. Two additional studies have also been carried out. These include prediction of ion secular frequency and ion trajectories at resonances in these traps.

In this numerical study, toroidal multipole coefficients of the respective traps are first evaluated and these are used for computing Mathieu parameters, a and q. These Mathieu parameters are used for constructing the stability plot, predicting secular frequency of ion motion and evaluating nonlinear resonances.

The stability regions of both the traps considered in this paper are qualitatively similar to the corresponding plot of the linear ion trap mass analyser. There are, however two significant differences. First, the stability plots for toroidal ion trap mass analysers have prominent resonances. Second the apices of the stability plots of the toroidal ion trap mass analysers are different from those of the linear ion trap mass analyser.

The secular frequency obtained using the Mathieu parameters in this paper agrees well with those obtained numerically, except close to the stability boundaries.

Finally, the prominent nonlinear resonances have been identified as $\beta_r = \frac{2}{3}$ and $\beta_z = \frac{2}{3}$ in both the traps. In one of the two traps there is an additional prominent nonlinear resonance at $\beta_r + \beta_z = 1$.

© 2016 Elsevier B.V. All rights reserved.

1. Introduction

A toroidal ion trap mass analyser can be viewed as a Linear Ion Trap (LIT) [8] curved around and connected at the ends or as a cross section of a Quadrupole Ion Trap (QIT) [1] rotated on edge to form the toroid [3,5]. These traps have a larger trapping volume and reduced space charge effects for a given trap radius and number of charges [3,8]. Toroidal ion traps come in broadly four different configurations. The first consists of symmetric hyperbolic electrodes [3], the second consists of asymmetric hyperbolic electrodes [3]. The third configuration is a simplified geometry with four cylindrical electrodes [2]. The final configuration is made of planar electrodes [5].

The stability of ions in ion trap mass analysers, such as the LIT [23] and the QIT [1], are obtained using the Mathieu parameters a and q [1]. In the ideal LIT, for instance, the Mathieu parameters a and q are given by [23]

$$a = \frac{4eU_{dc}}{m\Omega^2 r_0^2}, \tag{1}$$

$$q = \frac{2eV_{rf}}{m\Omega^2 r_0^2}, \tag{2}$$

where U_{dc} and V_{rf} are DC and RF potentials applied across the trap electrodes, Ω is angular frequency of RF drive, m and e are mass and charge of the ion, r_0 is the radius of the trapping volume.

The Mathieu stability plot delineates the region on the a-q plane where the ion motion in the two principal directions (x and y directions for the LIT and radial, r, and axial, z, directions for the QIT) are simultaneously stable. For the ideal traps, analytical expressions for the stability boundary are provided by the stable solutions of equation of ion motion, which has the form of Mathieu equation [1], in the two principal directions. When the traps have apertures

* Corresponding author at: Department of Computational and Data Sciences, Indian Institute of Science, Bangalore 560012, India.
E-mail addresses: appala@grads.cds.iisc.ac.in (A.N. Kotana), amohanty@cds.iisc.ac.in (A.K. Mohanty).

http://dx.doi.org/10.1016/j.ijms.2016.11.021
1387-3806/© 2016 Elsevier B.V. All rights reserved.

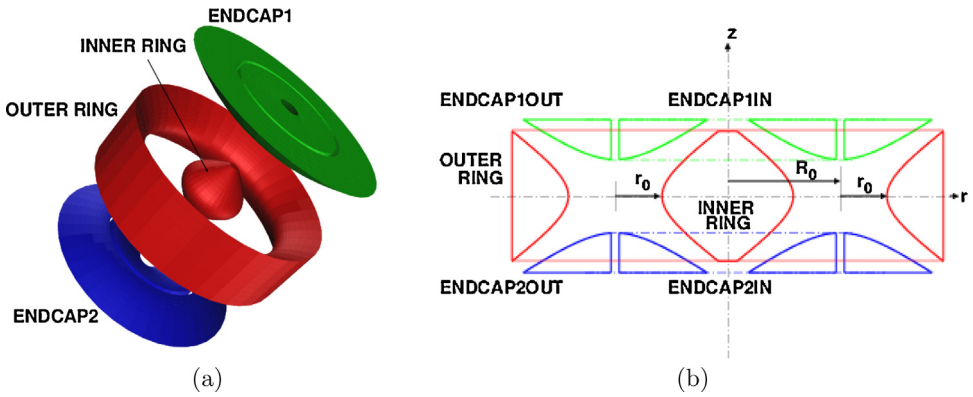

Fig. 1. Schematic view of the HypSymm obtained from symmetric QIT (with apertures on endcaps) rotated on edge to form the toroid. (a) Three dimensional view and (b) cross section in *rz*-plane.

and truncations or have simplified geometries such as the Rectilinear Ion Trap (RIT) [14] and the Cylindrical Ion Trap (CIT) [21] the Mathieu parameters are obtained using appropriate multipole coefficients. The multipole coefficients for the CIT are obtained by expanding the potential in terms of Legendre polynomials and for the RIT these are obtained by expanding the potential in terms of trigonometric functions. The *a*-*q* plane has also been used for depicting the stability of ions in traps which use non-sinusoidal waveforms for trapping ions, such as for depecting stability of ions in digital ion traps [35,37–42]. An alternative representation of stability diagram for quadrupole ion traps with additional quadrupolar excitation has also been discussed in the literature [36].

For an arbitrary toroidal ion trap mass analyser, however, there is no systematic method to generate the stability plot on the *a*-*q* plane. There are several reasons why the stability region for an arbitrary toroidal trap may be desired. For one, such plots would help in characterising the trap. Parameters such as q_{boundary}, the q values at which ions get destabilized in the mass selection boundary ejection method, can be obtained from such plots. Prominent resonances within the trap can also be obtained. This latter information would enable an experimenter to choose a specific nonlinear resonance for carrying out the resonance ejection studies. Finally, and perhaps importantly, such plots would enable comparison between traps within the toroidal trap family, something which has so far not been done. This last point's importance lies in the fact that in recent years several suggestions for different geometries for toroidal trap mass analysers have been proposed. Without such "normalised" plots on the *a*-*q* plane, evaluation of these geometries would not be possible to pick a candidate geometry for detailed experimental study.

This paper presents a method to construct Mathieu stability plot for any arbitrary toroidal ion trap mass analyser geometry.

To generate the stability plots for toroidal ion trap mass analysers, we rely on two studies, one by Higgs et al. [7] and the other being our own [26]. These studies have provided the means to describe potentials within the trap in terms of toroidal mutipole coefficients as well as the relationship between the toroidal multipole coefficients and the Mathieu parameters a and q.

Two arbitrary toroidal ion trap mass analyser geometries have been taken up for investigation in the present study. To make these simulations realistic, we have considered that the electrodes of the mass analysers have apertures and that the electrodes are truncated, a situation commonly encountered in practical traps. The technique we propose is general and is not restricted to the example geometries that we have considered in this study.

In the next section, the details of the two geometries have been selected for investigation are provided. In Section 3, the numerical methods used in this paper have been outlined. In Section 4, we present the results and discussion. Finally in Section 5 we present some concluding remarks.

2. Geometries considered

In this section we present two geometries that have been taken up for our study. These geometries are similar to the geometries presented by Lammert et al. [3]. Both the geometries have hyperbolic-shaped electrodes. However, one of these geometries has symmetric hyperbolic-shaped electrodes and another has asymmetric electrodes.

2.1. The geometry HypSymm

The first geometry considered will be referred to as HypSymm. This trap is obtained from symmetric QIT (with apertures on the endcaps) rotated on edge to form the toroid. The apertures on the endcaps of the QIT forms an annular shape apertures on endcaps of HypSymm. This geometry is similar to the symmetric trap considered by Lammert et al. [3]. While Lammert et al. [3] have used a stretched geometry QIT in our computations the QIT does not have any stretch. Fig. 1(a) shows its three dimensional view. Its cross section in *rz*-plane is shown in Fig. 1(b). R_0 is the distance from the origin to the mid-point between ring electrodes on the x-axis. r_0 is the half distance between ring electrodes.

The equations for electrodes in *rz*-plane are given in Table 1. In this table "Electrode" indicate the names of the electrodes shown in Fig. 1(b). $r(s)$ is parametric equation of radial component and $z(s)$ is parametric equation of axial component of the respective electrode. s_{min} and s_{max} are the minimum and maximum values of parameter s in the parametric equations of the respective electrode. The values of constants in these parametric equations are taken to be $R_0 = 0.024$ m, $r_0 = 0.01$ m, $\alpha_1 = 0.707$, $\alpha_2 = 0.707$ and $z_a = 0.00076$.

2.2. The geometry HypASymm

The second geometry considered will be referred to as HypASymm. This trap is obtained from asymmetric QIT (with

Table 1
Parametric equations of outer surfaces of the trap HypSymm in *rz*-plane.

Electrode	$r(s)$	$z(s)$	s_{min}	s_{max}
INNER RING	$R_0 - r_0\cosh(s)$	$\alpha_1 r_0 \sinh(s)$	−1.42	1.42
OUTER RING	$R_0 + r_0\cosh(s)$	$\alpha_1 r_0 \sinh(s)$	−1.42	1.42
ENDCAP1IN	$R_0 - r_0\sinh(s)$	$z_a + \alpha_1 r_0\cosh(s)$	0.09	1.42
ENDCAP1OUT	$R_0 + r_0\sinh(s)$	$z_a + \alpha_2 r_0\cosh(s)$	0.09	1.42
ENDCAP2IN	$R_0 - r_0\sinh(s)$	$-z_a - \alpha_1 r_0\cosh(s)$	0.09	1.42
ENDCAP2OUT	$R_0 + r_0\sinh(s)$	$-z_a - \alpha_2 r_0\cosh(s)$	0.09	1.42

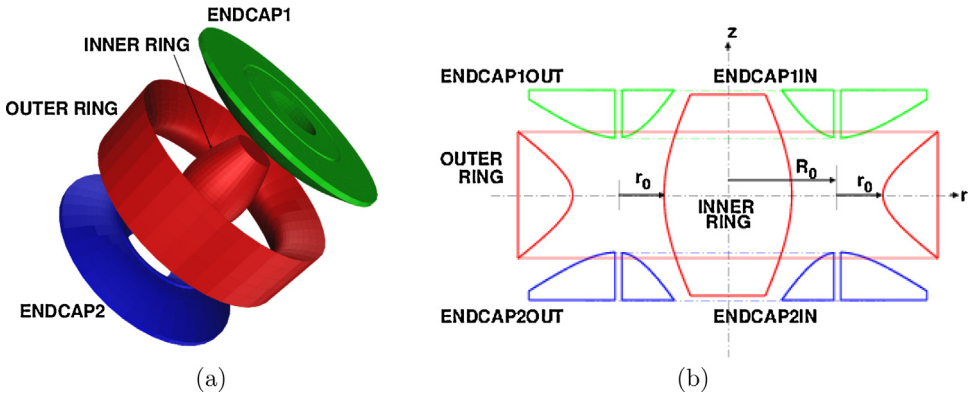

Fig. 2. Schematic view of the HypASymm obtained from asymmetric QIT (with apertures on endcaps) rotated on edge to form the toroid. (a) Three dimensional view and (b) cross-section in *rz*-plane.

Table 2
Parametric equations of outer surfaces of the trap HypASymm in *rz*-plane.

Electrode	$r(s)$	$z(s)$	s_{min}	s_{max}
INNER RING	$R_0 - r_0\cosh(s)$	$\alpha_1 r_0 \sinh(s)$	−1.03	1.03
OUTER RING	$R_0 + r_0\cosh(s)$	$\alpha_2 r_0 \sinh(s)$	−1.42	1.42
ENDCAP1IN	$R_0 - r_0\sinh(s)$	$z_a + \alpha_1 r_0 \cosh(s)$	0.07	1.03
ENDCAP1OUT	$R_0 + r_0\sinh(s)$	$-z_a + \alpha_2 r_0 \cosh(s)$	0.07	1.42
ENDCAP2IN	$R_0 - r_0\sinh(s)$	$-z_a - \alpha_1 r_0 \cosh(s)$	0.07	1.03
ENDCAP2OUT	$R_0 + r_0\sinh(s)$	$z_a - \alpha_2 r_0 \cosh(s)$	0.07	1.42

apertures on the endcaps) rotated on edge to form the toroid. The apertures on the endcaps of the QIT forms an annular shape apertures on endcaps of HypASymm. This trap too similar to the asymmetric trap considered by Lammert et al. [3]. Fig. 2(a) shows its three dimensional view. Its cross section in *rz*-plane is shown in Fig. 2(b). R_0 is the distance from the origin to the mid-point between ring electrodes on the *x*-axis. r_0 is the half distance between ring electrodes.

The equations for electrodes in *rz*-plane are given in Table 2. In this table "Electrode" indicate the names of the electrodes shown in Fig. 2(b). $r(s)$ is parametric equation of radial component and $z(s)$ is parametric equation of axial component of the respective electrode. s_{min} and s_{max} are the minimum and maximum values of parameter s in the parametric equations of the respective electrode. The values of constants in these parametric equations are taken to be $R_0 = 0.024$ m, $r_0 = 0.01$ m, $\alpha_1 = 1.8$, $\alpha_2 = 0.707$ and $z_a = -0.0054$.

3. Computational methods

The numerical methods used in the present study are described below.

3.1. The Boundary Element Method (BEM)

We use the Boundary Element Method (BEM) to calculate charge distribution on the surfaces of the electrodes of ion traps. We adopt the method outlined in Tallapragada et al. [20] to obtain charge distribution. Potential and electric field are obtained from the charge distribution.

3.2. Computation of ion trajectory

The trajectory of ion motion is computed by solving the following differential equations using Runge-Kutta fourth order method [29].

$$m\frac{d^2\mathbf{r}}{dt^2} = e\mathbf{E} \tag{3}$$

where m is mass of the ion; e is charge of the ion; $\mathbf{E}$ is electric field at time t and position $\mathbf{r}$. This is obtained as follows

$$\mathbf{E} = \left[U_{dc} + V_{rf}\cos(\Omega t)\right]\mathbf{E}_{quad} \tag{4}$$

where U_{dc} is DC potential; V_{rf} is RF potential; Ω is angular frequency of the RF drive; $\mathbf{E}_{quad}$ is the field at position $\mathbf{r}$ obtained by applying 0.5 V to ring electrodes and -0.5 V to endcap electrodes.

The computation of field $\mathbf{E}_{quad}$, using BEM is slower and the trajectory calculation using this, is further slower. In order to accelerate the computation we have used interpolated field in trajectory calculations. This kind of technique is already used by Wu et al. [21]. However our technique is slightly different in the following sense. We use BEM field to obtain interpolated field, where as they have used field obtained from finite difference method. Also in our method the computation of electric field close to electrodes is carried out with exact BEM.

In order to get interpolated field we select 100 by 100 grid in the rectangle having vertices $(0.95(R_0 - r_0), -0.95z_0)$, $(0.95(R_0 + r_0), -0.95z_0)$, $(0.95(R_0 - r_0), 0.95z_0)$ and $(0.95(R_0 + r_0), 0.95z_0)$ in *rz*-plane. At each of this grid points axial and radial components of electric field $\mathbf{E}_{quad}$ are computed using the BEM. The radial components are stored in one array and the axial components are stored in another array.

During the computation of trajectory at any time instant if the position of the ion (r, z) is inside the region covered by the above grid, the radial and axial components of $\mathbf{E}_{quad}$ are computed using the following equations

$$E_r^q = \eta_1 r + \eta_2 z + \eta_3 \tag{5}$$

$$E_z^q = \gamma_1 r + \gamma_2 z + \gamma_3 \tag{6}$$

where η_j and γ_j are unknown quantities to be determined. This method of computation is called linear interpolation. In order to obtain η_j and γ_j, we select three nearest neighbouring points to (r, z) on the grid. Let these points be (r_1, z_1), (r_2, z_2) and (r_3, z_3). and the stored electric fields at these points are (E_{r1}^q, E_{z1}^q), (E_{r2}^q, E_{z2}^q) and (E_{r3}^q, E_{z3}^q). The values of η_j are computed by solving the following system of equations

$$E_{r1}^q = \eta_1 r_1 + \eta_2 z_1 + \eta_3 \tag{7}$$

$$E_{r2}^q = \eta_1 r_2 + \eta_2 z_2 + \eta_3 \tag{8}$$

$$E_{r3}^q = \eta_1 r_3 + \eta_2 z_3 + \eta_3 \tag{9}$$

and the values of γ_j are computed by solving the following system of equations

$$E_{z1}^q = \gamma_1 r_1 + \gamma_2 z_1 + \gamma_3 \tag{10}$$

$$E_{z2}^q = \gamma_1 r_2 + \gamma_2 z_2 + \gamma_3 \tag{11}$$

$$E^q_{z3} = \gamma_1 r_3 + \gamma_2 z_3 + \gamma_3 \tag{12}$$

In case the point (r, z) is outside the region covered by the grid specified above we use the BEM to obtain the electric field.

In computation of stability region we use interpolated electric field whereas the trajectory computation for finding secular frequency of ion motion and trajectories at nonlinear resonances is done using exact BEM.

3.3. Determination of toroidal multipole coefficients

The potential in toroidal ion trap in terms of toroidal coordinates (σ, τ) [30] is of the form

$$\Psi(\sigma,\tau) = a_0\sqrt{\cosh\tau - \cos\sigma}\, Q_{-\frac{1}{2}}(\cosh\tau) + \sqrt{\cosh\tau - \cos\sigma} \times \sum_{\nu=1}^{\infty} [a_\nu \cos(\nu\sigma) + b_\nu \sin(\nu\sigma)]\, Q_{\nu-\frac{1}{2}}(\cosh\tau) \tag{13}$$

where $\Psi(\sigma, \tau)$ is potential at the point (σ, τ) and $Q_{\nu-\frac{1}{2}}(.)$ are associated Legendre functions of second kind [31]. a_ν and b_ν are toroidal multipole coefficients [26].

Three methods have been discussed in [26] for the determination of a_ν and b_ν. Of these methods, one method uses least square (LS) fit to the potentials obtained numerically on a grid of points in the trapping region. Another method uses Discrete Fourier Transform (DFT) of potentials that are obtained numerically on a constant τ circle within the trapping region. The remaining method uses surface charge distribution which is computed using the BEM. In this paper we have used the last method which uses surface charge distribution (referred as SC-BEM in [26]) to obtain the coefficients a_ν and b_ν.

3.4. Determination of the stability region

The stability region of a given geometry with fixed geometry parameters is found by the following procedure.

We consider a region consisting of a toroid having rectangular cross section enclosed by the trap electrodes. The trapping circle is assumed to lie within this region. $R_0 - r_0$ is lower bound, $R_0 + r_0$ is upper bound in radial direction of this region. Similarly $-z_0$ is lower bound and $+z_0$ is upper bound in axial direction. This region will define the region within which ion motion is considered to be stable. If amplitude of ion motion is equal to or larger than this limit, the motion is considered to be unstable.

All simulations have been carried out on an ion of mass to charge ratio of 78 Th with RF frequency 1 MHz. The initial conditions for all simulations are the same, namely, the position of the ion is on the trapping circle (considered to be the center of the trap) and the initial velocity has been set at 500 ms^{-1} in x-direction, 500 ms^{-1} in y-direction and 500 ms^{-1} in z-direction. This velocity is equivalent to 0.303 eV initial kinetic energy. The simulations have been carried out for different combinations of U_{dc} and V_{rf}, U_{dc} varying from -1000 V to 1000 V in steps of 1 V and V_{rf} varying from 0 to 2000 V_{0-p} in steps of 1 V_{0-p}. To check the stability of an ion, we begin with an initial value of U_{dc} and an initial value of V_{rf}. These values are inserted in Eq. (4) and the equation is solved using the fourth order Runge-Kutta method. The ion motion is allowed to evolve for 10 ms in steps of 10 ns. If within this 10 ms the amplitude of the ion motion equals or exceeds the region of stability, ion motion is labelled as "unstable". Else it is labelled as "stable". Once the initial combination of U_{dc} and V_{rf} has been checked for stability of ion motion, for the same value of U_{dc} a new value of V_{rf} is chosen and similarly check for stability. In this way the entire range of U_{dc} and V_{rf} are scanned for ion stability. The stored values of U_{dc} and V_{rf} for which stable motion is observed is used to compute the Mathieu parameters.

The Mathieu parameters are computed from U_{dc} and V_{rf} using [26] [1]

$$a_r = \frac{4eU_{dc}\lambda_1}{m\Omega^2} \tag{14}$$

$$q_r = -\frac{2eV_{rf}\lambda_1}{m\Omega^2} \tag{15}$$

$$a_z = -a_r \tag{16}$$

$$q_z = -q_r, \tag{17}$$

where a_r and q_r are related to x-direction ion motion, a_z and q_z are related to z-direction motion. The value of λ_1 in Eqs. (14) and (15) is given by

$$\lambda_1 = \frac{3\pi}{16a^2\sqrt{2}}\sqrt{(2a_0 - a_2)^2 + b_2^2}, \tag{18}$$

where a is the radius of the focal circle (the trapping circle), a_0, a_2 and b_2 are toroidal multipole coefficients [26]. Once these multipole coefficients are known, a numerical simulation of the stability region generated on a U_{dc}-V_{rf} plane can be converted to a-q plane.

The derivation details of Mathieu parameters defined in Eqs. (14) to (17) are discussed in [26]. The parameter λ_1 in these equations is dependent on the radius of the trapping circle, the toroidal multipole coefficients a_0, a_2 and b_2. The radius of the trapping circle is computed using the Newton method of root finding applied to electric field vector. The toroidal multipole coefficients are computed using the method is discussed in Section 3.3. These multipole coefficients are obtained with 0.5 V on ring electrodes and −0.5 V on endcap electrodes.

3.5. Secular frequency computation

In this paper, the secular frequency of ion motion is obtained in two independent methods and they are compared with each other.

In the first method the numerical trajectory of ion motion is determined. The trajectory is computed for 10 ms long using the Runge-Kutta fourth order method in steps of 10 ns. At initial step the ion is kept on the trapping circle in xz-plane with zero velocity in x, y-directions and 500 ms^{-1} in z-direction. In the computation of trajectory using Runge-Kutta method exact BEM field is used. From the numerical trajectory, the secular frequency is obtained with the open source program *harminv* [34,32,33]. Harminv has greater accuracy in extracting the frequencies compared to the Fast Fourier Transform (FFT) method [44] when the number of sinusoids present in the signal is small, as is the case in our simulations. We label this method as "Numerical" in the figures and text.

The second method uses the Mathieu parameters shown in Eqs. (16) and (17). Using these parameters the value of β_z [27] (the continued fraction approach for computing β_z in [1] will give the same result) is computed and the secular frequency of z-direction ion motion is given by

$$f_z = \frac{\beta_z}{2} f \tag{19}$$

where f is the frequency of the RF drive. This method of determination of secular frequency is denoted by "Predicted" in the figures.

[1] The Mathieu parameters a_r, q_r, a_z and q_z, in [26] are referred to $a_{Mathieu1}, q_{Mathieu1}, a_{Mathieu2}$ and $q_{Mathieu2}$ respectively, in this study.

3.6. Evaluation of nonlinear resonances

It will be seen in the results we present below that there are prominent regions within these plots where the ions are unstable. In order to evaluate what these nonlinear resonances are we take three points within each of these observed resonances, in both the traps, and compute respective β_r and β_z [1,27]. By using linear fit to these three values the equation of nonlinear resonance was found and assigned on the stability plots.

4. Results and discussions

In this section we present the results of our study. They have been divided into three sub sections, viz., (1) Stability region, (2) Secular frequency and (3) Nonlinear resonances. In each of these subsections the results of the two geometries, HypSymm and HypASymm, will be presented.

In our study we have taken the frequency of RF drive as f=1 MHz and the mass of ion is taken to be 78 Th. The trap dimensions have been given in Section 2.

4.1. Stability regions

The stability regions for the traps HypSymm and HypASymm are obtained using the method described in Section 3.4.

4.1.1. HypSymm

The stability region for the trap HypSymm in U_{dc}–V_{rf} plane is shown in Fig. 3. These values are then transformed into a–q plane using Eqs. (16) and (17). In these equations, the computation of Mathieu parameters a and q involve λ_1 shown in Eq. (18). Which requires toroidal multipole coefficients a_0, a_2 and b_2. These multipole coefficients are computed using the method described in Section 3.3 and are shown in Table 3. The computed Mathieu parameters are plotted in a plane with q_z along horizontal axis and a_z along vertical axis. This plot is shown in Fig. 4.

The last stable value of q_z along the line $a_z = 0$ is q_{boundary}. For the trap HypSymm $q_{\text{boundary}} = 0.889$.

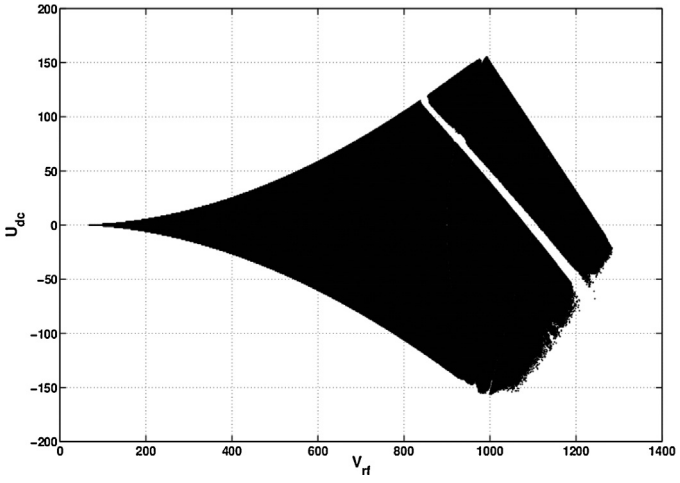

Fig. 3. Stability region of the trap HypSymm in terms of RF and DC potentials.

Table 3
Multipole coefficients for the traps HypSymm and HypASymm that are used to obtain Mathieu parameters.

Trap	a_0	a_2	b_2
HypSymm	−0.079	14.590	0
HypASymm	0.052	10.391	0

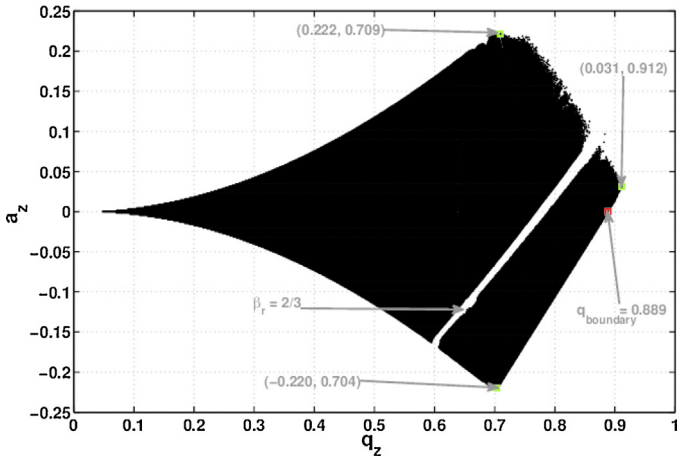

Fig. 4. Stability region of the trap HypSymm in terms of Mathieu parameters with marked apices and q_{boundary}.

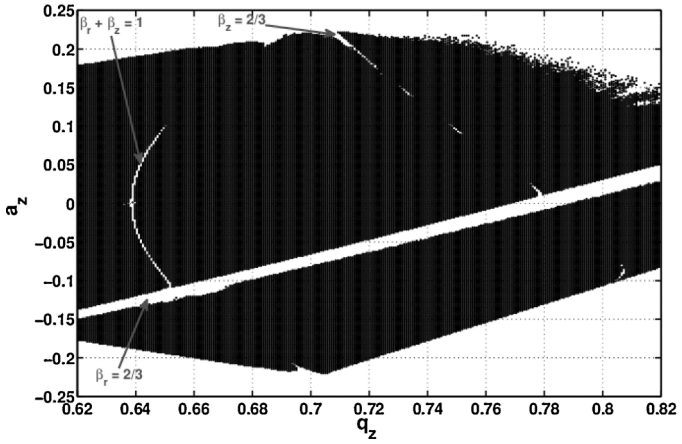

Fig. 5. Magnified view of portion in Fig. 4 that contains nonlinear resonances.

The (a_z, q_z) values of apices are (−0.220, 0.704) and (0.222, 0.709). The apex along the line $a_z = 0$ is shifted to (0.031, 0.921).

In order to see the prominent nonlinearities in the stability region a magnified view of of portion in Fig. 4 is shown in Fig. 5. It is evident from this figure that the prominent nonlinearities are along the curves $\beta_r = \frac{2}{3}$, $\beta_r + \beta_z = 1$ and $\beta_z = \frac{2}{3}$. These curves are obtained by the method described in Section 3.6. We have observed that along nonlinear resonance curves the ion ejection occurs in the radial direction for the initial conditions chosen in our study.

4.1.2. HypASymm

The stability region for the trap HypASymm in U_{dc}-V_{rf} plane is shown in Fig. 6. These values are then transformed into a-q plane using Eqs. (16) and (17). In these equations, the computation of Mathieu parameters a and q involve λ_1 shown in Eq. (18). Which requires toroidal multipole coefficients a_0, a_2 and b_2. These multipole coefficients are computed using the method described in Section 3.3 and are shown in Table 3. The computed Mathieu parameters are plotted in a plane with q_z along horizontal axis and a_z along vertical axis. This plot is shown in Fig. 7. It is to be noted that the stability region of the trap HypASymm is much more symmetric with respect to $a_z = 0$ axis when it is compared to the trap HypSymm. Also the boundaries of stability region of the trap HypASymm are smoother in comparison to the stability region of the trap HypSymm. In the stability region of HypASymm, only two nonlinear resonance curves are observed.

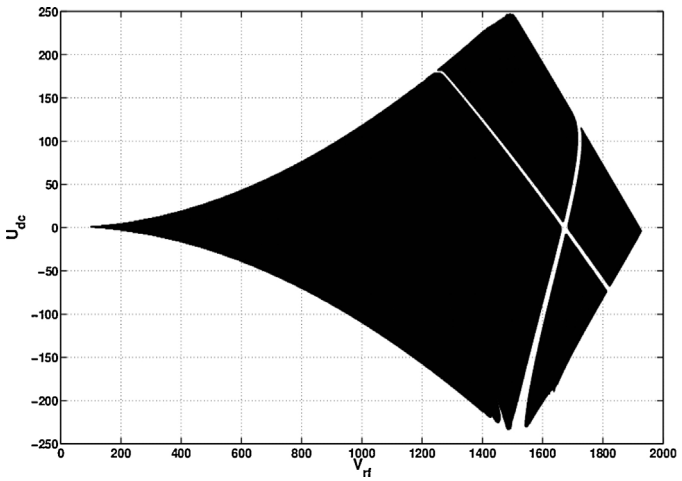

Fig. 6. Stability region of the trap HypASymm in terms of RF and DC potentials.

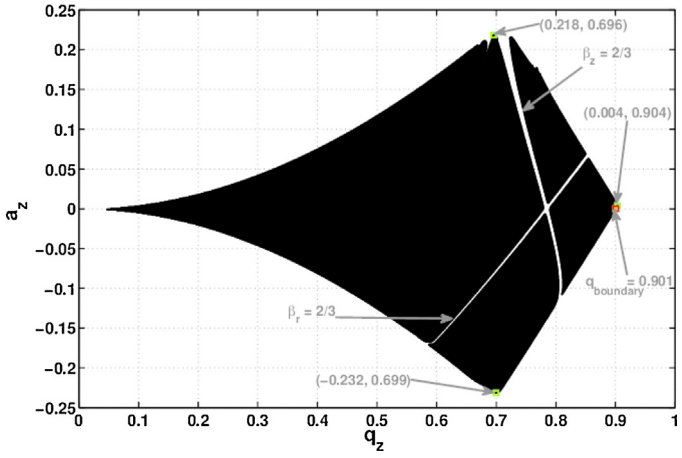

Fig. 7. Stability region of the trap HypASymm in terms of Mathieu parameters with marked nonlinear resonances, apices and q_{boundary}.

The last stable value of q_z along the line $a_z = 0$ is q_{boundary}. For the trap HypASymm $q_{\text{boundary}} = 0.901$.

The (a_z, q_z) values of apices are (−0.232, 0.699) and (0.218, 0.696). The apex along the line $a_z = 0$ is shifted to (0.004, 0.904). This shift is much smaller in comparison to the shift in the trap HypSymm.

It is evident from the stability region shown in Fig. 7, that the prominent nonlinearities are along the curves $\beta_r = \frac{2}{3}$ and $\beta_z = \frac{2}{3}$. These curves are obtained by the method described in Section 3.6. It is to be noted that the nonlinear resonance $\beta_r + \beta_z = 1$ is not present for this trap, which was there for the trap HypSymm. We have observed that along nonlinear resonance curves the ion ejection occurs in the radial direction for the initial conditions chosen in our study.

In summary q_{boundary}, the apices, and the apex along the line $a_z = 0$ for the traps HypSymm and HypASymm are presented in Table 4.

Table 4
Apices (a_z, q_z) and q_{boundary} for HypSymm and HypASymm.

Trap	Lower apex	Upper apex	Right apex	q_{boundary}
HypSymm	(−0.220, 0.704)	(0.222, 0.709)	(0.031, 0.921)	0.889
HypASymm	(−0.232, 0.699)	(0.218, 0.696)	(0.004, 0.904)	0.901

4.2. Secular frequency

In this section, the secular frequencies obtained using both the methods described in the Section 3.5, will be compared for the traps HypSymm and HypASymm. In the first method the Mathieu parameters a and q will be used to compute the secular frequency. This will be compared with the secular frequency obtained numerically.

4.2.1. HypSymm

In order to compare the secular frequencies with "Predicted" secular frequencies we need Mathieu parameters. The computation of Mathieu parameters involve λ_1 shown in Eq. (18). This parameter λ_1 is computed using the multipole coefficients shown in Table 3. Once the Mathieu parameters are known the value of β_z is computed. From which the "Predicted" secular frequencies are obtained using Eq. (19).

The secular frequencies obtained using Mathieu parameters are shown in Fig. 8. In which Fig. 8(a) shows comparison of numerical and predicted secular frequencies. In this plot q_z is shown along horizontal axis and secular frequencies are presented along vertical axis. It should be noted that there is good match between numerical secular frequencies and predicted secular frequencies. It is observed that there is a gap in Fig. 8(a), which can be seen clearly in inset. This gap is due to the unstable motion of ion in that region. The ratio of the RF potentials at the gap to the boundary is 0.864. This ratio is close to the ratio 0.85 observed by Higgs and Austin [7] for pure quadrupole toroidal ion trap. The Mathieu parameter at the gap is $q_z = 0.784$ and at the boundary $q_z = 0.907$.

It is to be noted that from the discussion of stability region of the trap HypSymm presented in Section 4.1.1, $q_{\text{boundary}} = 0.889$. This value is slightly lower than the present value 0.907. This is because in the present case, the initial velocities in x and y-direction are zero and 500 ms^{-1} in z-direction. Where as in Section 4.1.1 the initial velocity in all x, y and z-directions is 500 ms^{-1}. That is the initial kinetic energy of ion for generating stability regions is higher, in comparison to the initial kinetic energy for generating secular frequencies. Hence there is a slight shift in the boundary.

Fig. 8(b) shows percentage of relative error in "Predicted" secular frequency in comparison to "Numerical" secular frequency. In this plot q_z is shown along horizontal axis and percentage of error relative to numerical secular frequency is presented along vertical axis. The presence of this error is due to nonlinearities in the field. The error is larger at lower q_z values and near boundary. The larger error in the frequency for smaller q_z values is possibly due to larger oscillation amplitudes. Which is due to weak field at smaller q_z values in comparison to larger q_z values. Near the boundary the ion will have larger oscillation amplitudes as it is close to instability. Which in turn cause larger error in the predicted frequency.

4.2.2. HypASymm

In order to compare the secular frequencies with "Predicted" secular frequencies we need Mathieu parameters. The computation of Mathieu parameters involve λ_1 shown in Eq. (18). This parameter λ_1 in these equations is computed using the multipole coefficients shown in Table 3. Once the Mathieu parameters are known the value of β_z is computed. From which the "Predicted" secular frequencies are obtained using Eq. (19).

The secular frequencies obtained using Mathieu parameters are shown in Fig. 9. In which Fig. 9(a) shows comparison of numerical and predicted secular frequencies. In this plot q_z is shown along horizontal axis and secular frequencies are presented along vertical axis. It should be noted that there is good match between numerical secular frequency and predicted secular frequency. It is observed that there is a gap in Fig. 9(a), which can be seen clearly in inset. This gap is due to the unstable motion of ion in that region. The ratio of the RF potentials at the gap to the boundary is 0.863. Here

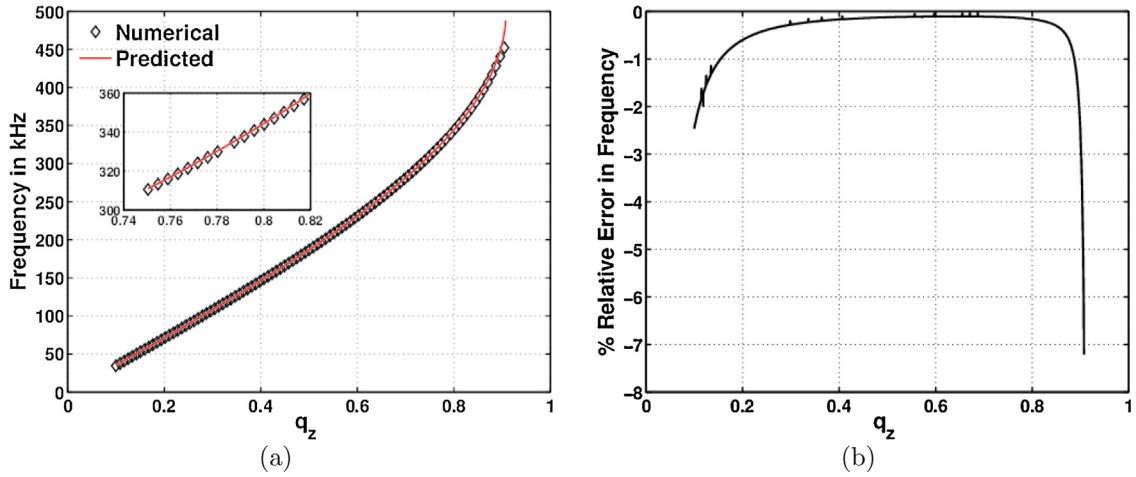

Fig. 8. Secular frequency variation in the trap HypSymm versus q_z. (a) Comparison of secular frequency obtained using q_z (denoted by "Predicted") with numerically obtained frequency (denoted by "Numerical"). (b) Percentage of relative error in "Predicted" secular frequency with respect to "Numerical" secular frequency.

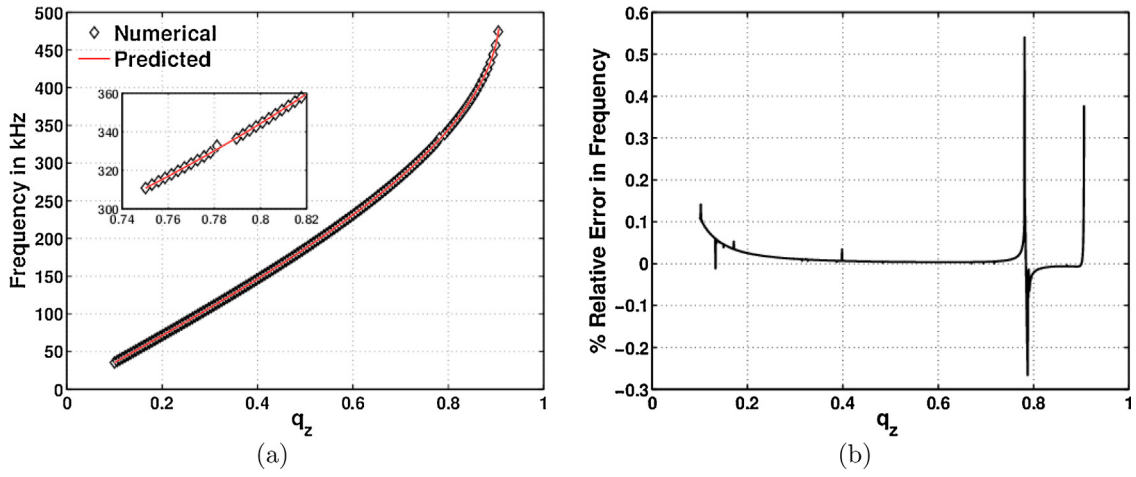

Fig. 9. Secular frequency variation in the trap HypASymm versus q_z. (a) Comparison of secular frequency obtained using q_z (labelled as "Predicted") with numerically obtained frequency (labelled as "Numerical"). (b) Percentage of relative error in "Predicted" secular frequency with respect to "Numerical" secular frequency.

too, this ratio is close to the ratio 0.85 observed by Higgs and Austin [7] for pure quadrupole toroidal ion trap. The Mathieu parameter at the gap is $q_z = 0.782$ and at the boundary $q_z = 0.905$.

It is to be noted that from the discussion of stability region of the trap HypASymm presented in Section 4.1.2, $q_{\text{boundary}} = 0.901$. This value is slightly lower than the present value 0.905. This is because in the present case, the initial velocities in x and y-direction are zero and 500 ms^{-1} in z-direction. Where as in Section 4.1.2 the initial velocity in all x, y and z-directions is 500 ms^{-1}. That is the initial kinetic energy of ion for generating stability regions is higher, in comparison to the initial kinetic energy for generating secular frequencies. Hence there is a slight shift in the boundary.

Fig. 9(b) shows percentage of relative error in "Predicted" secular frequency in comparison to "Numerical" secular frequency. In this plot q_z is shown along horizontal axis and percentage of error relative to numerical secular frequency is presented along vertical axis. The presence of this error is due to nonlinearities in the field. The error is larger at lower q_z values and near boundary. The larger error in the frequency for smaller q_z values is possibly due to larger oscillation amplitudes. Which is due to weak field at smaller q_z values in comparison to larger q_z values. Near the boundary the ion will have larger oscillation amplitudes as it is close to instability. Which in turn cause larger error in the predicted frequency. However the error is quite small in comparison to the trap HypSymm. This is because the field inhomogeneities in the trap HypASymm are smaller in comparison to the trap HypSymm.

4.3. Nonlinear resonances

In this section we will show plots of the ion trajectories in the radial (both x and y) and z-directions as well as on the xz-plane. These trajectories are plotted at the point on the gap shown in the Fig. 8(a) for the trap HypSymm and Fig. 9(a) for the trap HypASymm. This is done to confirm that the ion ejection does indeed occur in this region. As mentioned earlier, the mass of the ion is taken to be 78 Th. The initial position of the ion is kept on trapping circle in xz-plane. The initial velocity in x, y-directions is kept at 0 ms^{-1} and the initial velocity in the z-direction is taken to be 500 ms^{-1}.

4.3.1. HypSymm

The trajectory at $q_z = 0.784$ (corresponding to $U_{\text{dc}} = 0$ and $V_{\text{rf}} = 1105\ V_{0-p}$) in the trap HypSymm is shown in Fig. 10. The trajectory along x-direction is shown in Fig. 10(a) and the last few cycles of trajectory are shown in inset. This trajectory shows increase in the amplitude of x-direction motion and finally ion ejection takes place after 800 μs. The direction of ejection is radially outward as can be seen from the last few cycles of the trajectory shown in inset of x-direction trajectory. The y-direction trajectory is shown

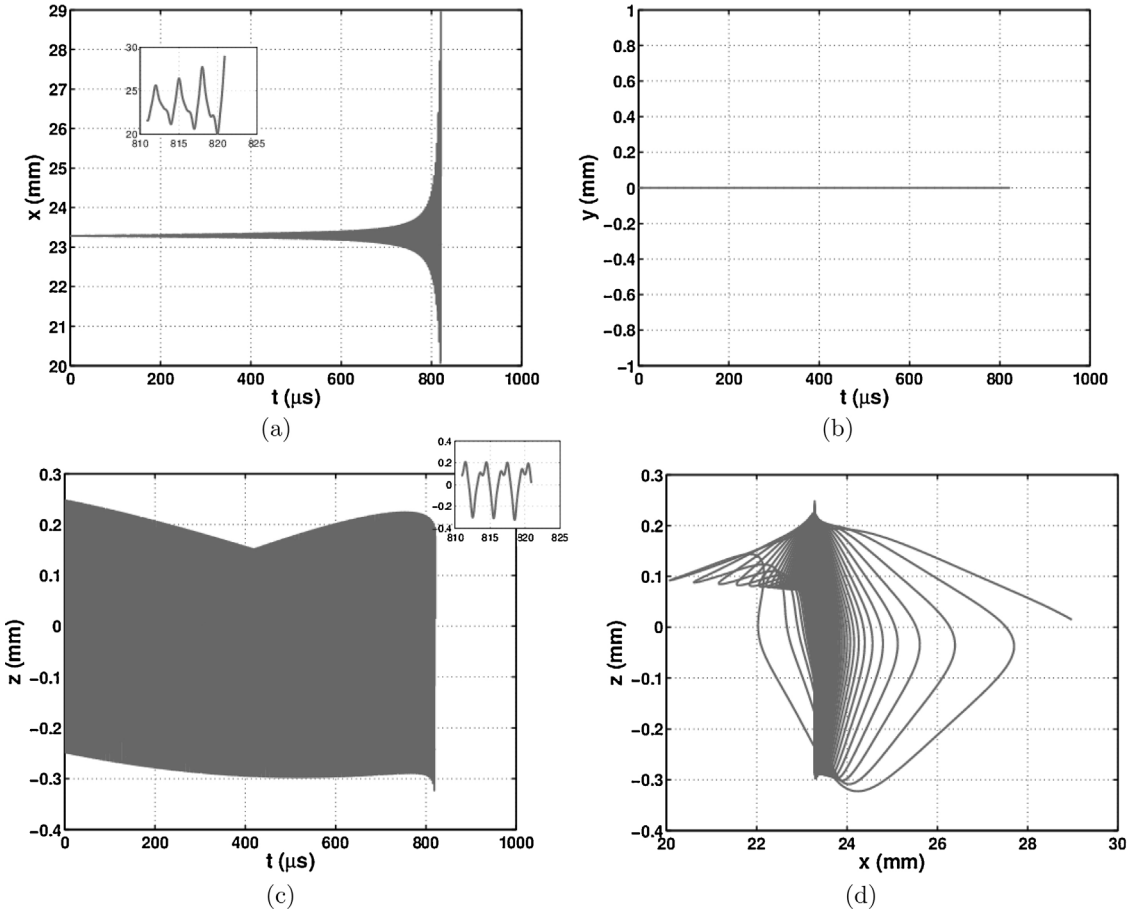

Fig. 10. Ion trajectory evolution in HypSymm. (a) x-direction trajectory with respect to time, (b) y-direction trajectory with respect to time, (c) z-direction trajectory with respect to time and (d) trajectory in xz-plane.

in Fig. 10(b). This plot shows that there is no evolution in the amplitude along y-direction. The z-direction trajectory is shown in Fig. 10(c) and last few cycles of the trajectory are shown in inset. It can be concluded from the last few cycles of the trajectory shown in inset that the ion is stable along z-direction. Also the amplitude of ion motion from the trapping center remain within 0.3 mm. The trajectory in xz-direction is shown in Fig. 10(d). This figure also indicates that the ion ejection occurs in the radial (x) direction.

It should be noted that $q_z = 0.784$ give $\beta_z = \frac{2}{3}$. Which is similar to nonlinear resonance point in the trap QIT having cubic term in the potential or quadratic term in the field [10,43].

4.3.2. HypASymm

The trajectory at $q_z = 0.785$ (corresponding to $U_{dc} = 0$ and $V_{rf} = 1675\,V_{0-p}$) in the trap HypASymm is shown in Fig. 11. The trajectory along x-direction is shown in Fig. 11(a) and the last few cycles of trajectory are shown in inset. This trajectory shows increase in the amplitude of x-direction motion and finally ion ejection takes place after 350 μs. The direction of ejection is radially inward as can be seen from the last few cycles of the trajectory shown in inset of x-direction trajectory. The y-direction trajectory is shown in Fig. 11(b). This plot shows that there is no evolution in the amplitude along y-direction. The z-direction trajectory is shown in Fig. 11(c) and last few cycles of the trajectory are shown in inset. Similar to x-direction motion, here too the amplitude of ion motion in z-direction increases. However, the ion is stable in z-direction. This can be seen from last few cycles of z-direction trajectory shown in the inset of Fig. 11(c). The trajectory in xz-direction is shown in Fig. 11(d). This figure also indicates that the ion amplitude increases in x-direction as well as in z-direction.

5. Concluding remarks

This paper presents a method to delineate the regions of stability of toroidal ion trap mass analysers on the a-q plane. Two toroidal trap mass analysers, labelled as HypSymm and HypASymm are considered. In addition to evaluating the stability region, we have also carried out two other studies, which includes prediction of secular frequencies and ion trajectories at resonances.

For computing stability region, the combination of U_{dc} and V_{rf} values for which ion motion is stable is first obtained. These potentials are transformed into a and q values using Eqs. (16) and (17) for the given trap.

The stability plots of both the traps have regions of nonlinear resonances along $\beta_r = \frac{2}{3}$ and $\beta_z = \frac{2}{3}$. In addition to these, the nonlinear resonance curve $\beta_r + \beta_z = 1$ for the trap HypSymm is also present. These resonances occur possibly due to hexapole and octopole contributions to the field in the toroidal ion traps. In order to confirm this further investigation is required.

In the second study we have compared secular frequencies along $U_{dc} = 0$ line obtained from obtained from the Mathieu parameters with those obtained numerically. It is observed that there is a good match of the frequency obtained using the Mathieu parameters a and q with those obtained numerically.

In the third study we have presented trajectories of ion motion at the nonlinear resonance point $q_z = 0.784$ (HypSymm) and $q_z = 0.785$

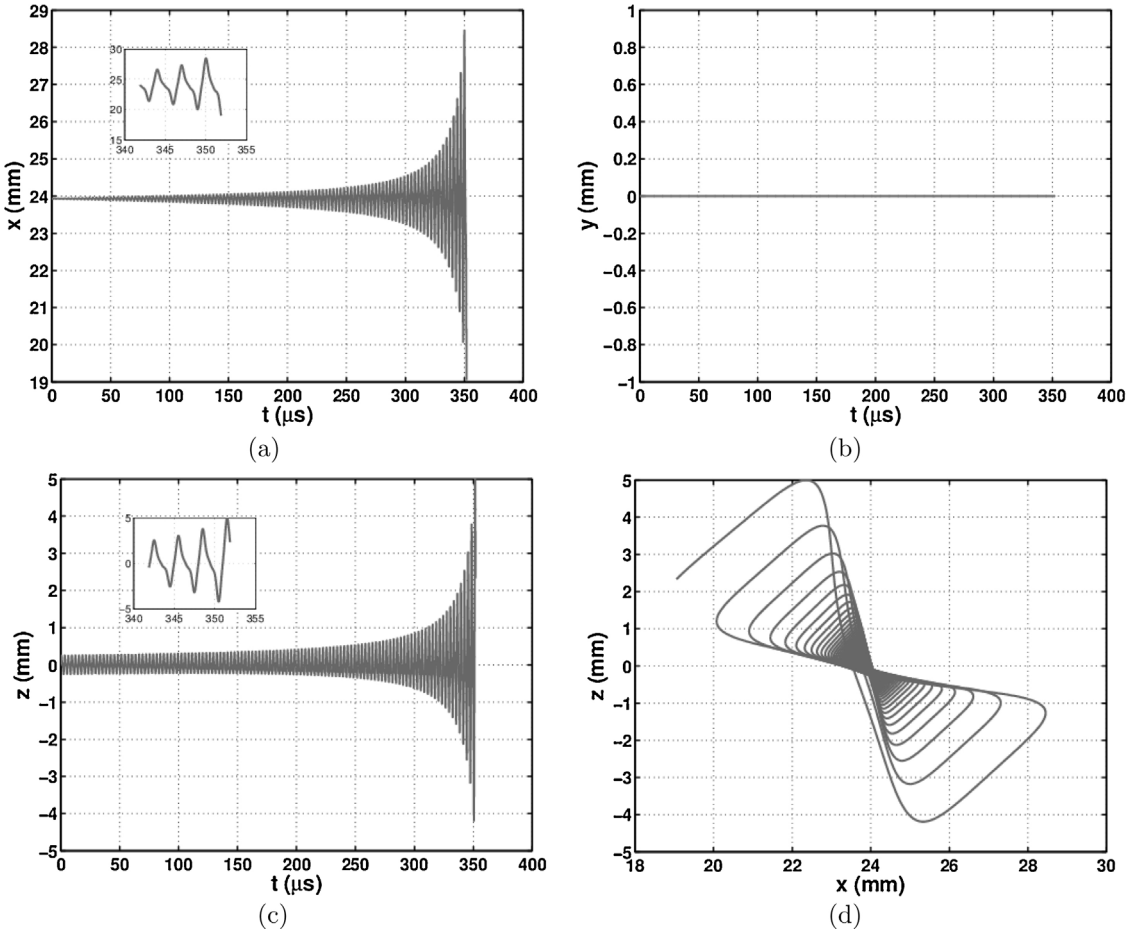

Fig. 11. Ion trajectory evolution in HypASymm. (a) *x*-direction trajectory with respect to time, (b) *y*-direction trajectory with respect to time, (c) *z*-direction trajectory with respect to time and (d) trajectory in *xz*-plane.

(HypASymm). These trajectories indicate that the ion ejection occurs in the radial direction for the initial conditions chosen in our study.

Some general observations can be made on the basis of our study. The stability regions of both the traps considered in this paper are qualitatively similar to the corresponding plot of the LIT, but there are two significant differences. The most important difference is the presence of gaps in the stability regions of the two toroidal traps compared to the stability region for the ideal LIT. A second difference is that the apices are also different, more for HypSymm than for HypASymm.

Acknowledgements

We thank Professor A.G. Menon for discussions during the preparation of this manuscript. We thank the two anonymous reviewers for their comments which have improved the manuscript.

References

[1] R.E. March, R.J. Hughes, Quadrupole Storage Mass Spectrometry, Wiley-Interscience, New York, 1989.
[2] N. Taylor, D.E. Austin, A simplified toroidal ion trap mass analyzer, Int. J. Mass Spectrom. 321 (2012) 25–32.
[3] S.A. Lammert, W.R. Plass, C.V. Thompson, M.B. Wise, Design, optimization and initial performance of a toroidal RF ion trap mass spectrometer, Int. J. Mass Spectrom. 212 (2001) 25–40.
[5] D.E. Austin, M. Wang, S.E. Tolley, J.D. Maas, A.R. Hawkins, A.L. Rockwood, H.D. Tolley, E.D. Lee, M.L. Lee, Halo Ion Trap Mass Spectrometer, Anal. Chem. 79 (2007) 2927–2932.
[7] J.M. Higgs, B.V. Petersen, S.A. Lammert, K.F. Warnick, D.E. Austin, Radiofrequency trapping of ions in a pure toroidal potential distribution, Int. J. Mass Spectrom. 395 (2016) 20–26.
[8] M.E. Bier, J.E.P. Syka, 1995. Ion trap mass spectrometer system and method, U.S. Patent No. 5,420,425 A.
[10] Y. Wang, J. Franzen, K.P. Wanczek, The non-linear resonance ion trap. Part 2. A general theoretical analysis, Int. J. Mass Spectrom. Ion Process. 124 (1993) 125–144.
[14] A. Krishnaveni, Neeraj Kumar Verma, A.G. Menon, A.K. Mohanty, Numerical observation of preferred directionality in ion ejection from stretched rectilinear ion traps, Int. J. Mass Spectrom. 275 (2008) 11–20.
[20] P.K. Tallapragada, A.K. Mohanty, A. Chatterjee, A.G. Menon, Geometry optimization of axially symmetric ion traps, Int. J. Mass Spectrom. 264 (2007) 38–52.
[21] G. Wu, R.G. Cooks, Z. Ouyang, Geometry optimization for the cylindrical ion trap: field calculations, simulations and experiments, Int. J. Mass Spectrom. 241 (2005) 119–132.
[23] P.H. Dawson, Quadrupole Mass Spectrometry and its Applications, Elsevier, Amsterdam, 1976.
[26] Appala Naidu Kotana, A.K. Mohanty, Determination of multipole coefficients in toroidal ion trap mass analysers, Int. J. Mass Spectrom. 408 (2016) 62–76.
[27] E.T. Whittaker, G.N. Watson, A Course of Modern Analysis, 4th ed., Cambridge University Press, Cambridge, 1927.
[29] K. Atkinson, An Introduction to Numerical Analysis, 2nd ed., John Wiley, New York, 1989.
[30] P.M. Morse, H. Feshbach, Methods of Theoretical Physics, Part I, McGraw-Hill, New York, 1953.
[31] P.M. Morse, H. Feshbach, Methods of Theoretical Physics, Part II, McGraw-Hill, New York, 1953.
[32] V.A. Mandelshtam, H.S. Taylor, Harmonic inversion of time signals and its applications, J. Chem. Phys. 107 (1997) 6756–6769.
[33] V.A. Mandelshtam, FDM: the filter diagonalization method for data processing in NMR experiments, Progr. Nucl. Magn. Reson. Spectrosc. 38 (2001) 159–196.

[34] V.A. Mandelshtam. http://ab-initio.mit.edu/wiki/index.php/Harminv.
[35] S. Bandelow, G. Marx, L. Schweikhard, The 3-state digital ion trap, Int. J. Mass Spectrom. 353 (2013) 49–53.
[36] A. Vernier, F. Chirot, R. Antoine, A. Salvador, J.P. Charrier, J. Lemoine, P. Dugourd, Alternative representation for the stability diagram of quadrupole ion traps upon additional quadrupolar excitation, Eur. J. Mass Spectrom. 19 (2013) 141–149.
[37] L. Ding, M. Sudakov, S. Kumashiro, A simulation study of the digital ion trap mass spectrometer, Int. J. Mass Spectrom. 221 (2002) 117–138.
[38] S. Bandelow, G. Marx, L. Schweikhard, The stability diagram of the digital ion trap, Int. J. Mass Spectrom. 336 (2013) 47–52.
[39] G.F. Brabeck, P.T.A. Reilly, Mapping ion stability in digitally driven ion traps and guides, Int. J. Mass Spectrom. 364 (2014) 1–8.
[40] P.T.A. Reilly, G.F. Brabeck, Mapping the pseudopotential well for all values of the Mathieu parameter q in digital and sinusoidal ion traps, Int. J. Mass Spectrom. 392 (2015) 86–90.
[41] G.F. Brabeck, Computational analysis of quadrupole mass filters employing nontraditional waveforms, J. Am. Soc. Mass Spectrom. 27 (2016) 1122–1127.
[42] G.F. Brabeck, H. Koizumi, E. Koizumi, P.T.A. Reilly, Characterization of quadrupole mass filters operated with frequency-asymmetric and amplitude-asymmetric waveforms, Int. J. Mass Spectrom. 404 (2016) 8–13.
[43] R. Alheit, S. Kleineidam, F. Vedel, M. Vedel, G. Werth, Higher order non-linear resonances in a Paul trap, Int. J. Mass Spectrom. Ion Process. 154 (1996) 155–169.
[44] E. Chu, Discrete and Continuous Fourier Transforms: Analysis, Applications and Fast Algorithms, Chapman and Hall/CRC, United Kingdom, 2008.